Endoscopic diffraction phase microscopy

Chenfei Hu,[1] [ID] Shuaishuai Zhu,[1,2] Liang Gao,[1] and Gabriel Popescu[1,*]

[1]*Electrical and Computer Engineering, Beckman Institute for Advanced Science and Technology, University of Illinois at Urbana-Champaign, Urbana, Illinois 61801, USA*
[2]*Harbin Institute of Technology, Center of Ultraprecision Optoelectronic Instrument, Harbin 150001, China*
Corresponding author: gpopescu@illinois.edu

In this Letter, we present, to our knowledge, the first endoscopic diffraction phase microscopy (eDPM) system. This instrument consists of a gradient-index-lens-based endoscope probe followed by a DPM module, which enables single-shot phase imaging at a single-cell-level resolution. Using the phase information provided by eDPM, we show that the geometric aberrations associated with the endoscope can be reduced by digitally applying a spectral phase filter to the raw data. The filter function is a linear combination of polynomials with weighting optimized to improve resolution. We validate the principle of the proposed method using reflective semiconductor samples and blood cells. This research extends the current scope of quantitative phase imaging applications, and proves its potential for future *in vivo* studies.   © 2018 Optical Society of America

Optical endoscopic imaging allows visualization of tissue microenvironment, and plays an important clinical role for diagnosing, guiding endo-surgery, and monitoring treatment and recovery [1]. Compared to other standard clinical tomographic imaging modalities (i.e., ultrasound, CT, MRI, and nuclear medicine), optical techniques are complementary in terms of high spatial resolution, contrast, noninvasiveness, portability, and cost. Because of the opaque nature of soft tissue, one needs to introduce either intrinsic or exogenous contrast mechanisms to identify abnormal or diseased tissue [2]. Auto-fluorescent imaging [3], exogenous fluorescence imaging [4,5], and non-linear optical endoscopy [6–8] utilize molecular absorption followed by emission as a contrast mechanism. Photoacoustic endoscopy uses optical absorption to produce ultrasound and high-contrast volumetric images [9,10]. Optical coherence tomography (OCT), built upon the principle of low-coherence interferometry, measures the sample's depth-resolved scattering signature, and holds broad endoscopic applicability [11]. In fluorescence imaging, due to the difference in data processing, the reported sensitivity and specificity in identifying malignant tumors or abnormal tissue vary significantly [12]. Nonlinear optical methods generally require a point-scanning mechanism

and high-power laser for efficient excitation [6]. Commonly used OCT systems also require 2D scanning to produce *en face* images [13,14].

Quantitative phase imaging (QPI) is an emerging label-free imaging modality, receiving increased attention in the past decade. QPI employs interferometry to precisely measure the optical pathlength difference across the specimen, which then serves as an intrinsic contrast parameter [15]. This modality is very effective in visualizing extremely transparent objects, such as single cells [16–19]. Due to its capabilities of label-free imaging and nanometer-scale sensitivity, QPI is a valuable tool for mapping 3D structures [20–22] and measuring activities in living cells [23–26]. While most existing QPI systems measure samples *in vitro* or *ex vivo*, the study of endoscopic QPI research or *in vivo* QPI imaging systems is rarely explored, to our knowledge [27–29]. In this research, we describe an endoscopic QPI system in free space. This system combines an endoscope probe based on a gradient index (GRIN) lens and a diffraction phase microscopy (DPM) [30] module. We demonstrate, for the first time to our knowledge, that QPI can be performed through an endoscope. We also show that, unlike most common geometries in which the endoscope transfers coherently the field of view (FOV), one can instead transfer the spatial frequency space. This way, the numerical aperture of the endoscope does not limit the spatial resolution, but, rather, the FOV. We obtain the system impulse response at each spatial position in the FOV, allowing for aberration correction. Finally, we demonstrate the principle of the technique with semiconductor (reflective) samples and blood cells.

The endoscopic DPM (eDPM) system is shown in Fig. 1. The endoscope is essentially a microscope working in a reflection geometry. For the illumination geometry, the light from a halogen lamp is coupled into a multimode fiber and guided to the tip of the probe. The illumination field is reflected by a right-angle prism and passes through an objective. In the imaging path, the back-reflected light from the sample is collected, and then a doublet lens, Lens 3, images the back focal plane of the objective and forms an intermediate image of the Fourier plane at distal surface of the GRIN lens, which duplicates the image at its proximal surface. The right-angle prism, L3, and the GRIN lens were cemented together as a complete unit with a total length approximately 230 mm and a clear aperture diameter <10 mm, with details discussed in an earlier research [31].
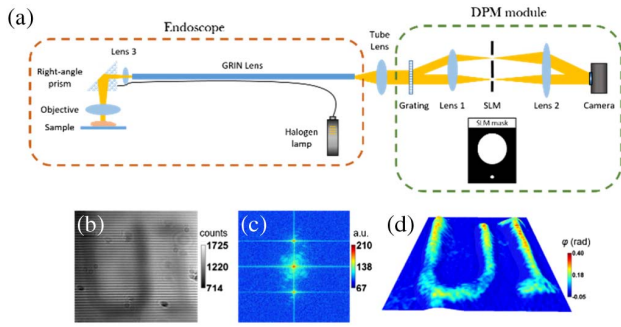
Fig. 1. Endoscopic DPM system. (a) The endoscope is a reflective microscope, and DPM module is a common-path, off axis. (b) Interferogram captured by the camera. Using a Hilbert transform (c), a quantitative phase map (d) is obtained [32].

To proof the principle of concept, we use a microscope objective [10 × /NA (numerical aperature) = 0.3], and the distance between the objective and prism is roughly 60 mm. After passing through the tube lens, we obtain an image conjugate to the sample field. At the image plane, we placed the DPM module, as follows. A diffraction grating (110 grooves/mm) splits the image field into multiple diffraction orders, each containing the full information about the sample. The zeroth- and first-order beams are isolated at the Fourier plane using a spatial light modulator (SLM). The zeroth order is spatially low-passed to create a DC reference field, while we allow the first order to pass completely and form the sample field. The diameter of the pinhole filter is approximately 200 μm. The camera (Nikon DS-Qi1) records an interferogram between the two diffraction beams, and a phase map is reconstructed via a Hilbert transform, the details of which are well discussed in Ref. [32]. Limited by the power of light source, the acquisition speed is ~1 frame/s.

In the earlier endoscope probe design [31], Lens 3 worked as the imaging component, and the GRIN lens as the relay unit, which yields a system NA of 0.02 [Fig. 2(a)]. As demonstrated in Fig. 2(b), after adding the objective, this system aperture limits the size of the FOV, while the resolution is determined by the objective.

In order to characterize the system performance, we measure the phase response of a moving edge, as follows. A piece of GaAs wafer with a rectangular pattern was placed on the sample plane. Let us consider the phase edge described by a (phase) step function,
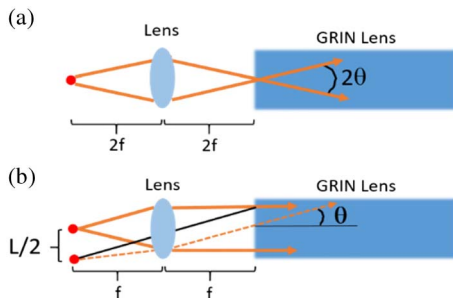

Fig. 2. Objective lens images the object (a) and the Fourier plane (b) after adding the objective.

$$\phi(x) = \phi(0)\Gamma(x), \tag{1}$$

where $\Gamma(x)$ is the Heaviside (step) function,

$$\Gamma(x) = \begin{cases} 1 & x > 0 \\ 1/2 & x = 0 , \\ 0 & x < 0 \end{cases} \tag{2}$$

and ϕ_0 is the phase height of the step. In our case, we used a GaAs wafer with a profile of $h = 76.8$ nm, such that in reflection, it yields $\phi_0 = 2\frac{2\pi}{\lambda}h = 1.4$ rad [33]. Through our imaging system, the phase is smoothed out to

$$\varphi(x) = \phi(x)\otimes\text{PSF}(x), \tag{3}$$

where PSF is the point spread function of our system, and $\otimes$ is the convolution operation along the x-axis. By moving this sample across the FOV, we can measure the response at every spatial location, and then obtain the spatially dependent edge response, $\varphi(x - x')$ [Figs. 3(a)–3(c)]. Because the sample is illuminated by partially coherent light, the measured phase, $\phi_i(r)$, misses certain low-frequency components, as shown in Fig. 3(a). The effect of illumination on the measured phase map ϕ_i can be formulated as [34]

$$\phi_i(r) \approx \varphi(r) - \varphi(r)\otimes_r h_i(r) = \varphi(r)\otimes_r[\delta(r) - h_i(r)], \tag{4}$$

where $\varphi(r)$ is the "ideal" measured phase under the conditions of perfect coherence, $h_i(r)$, the normalized spatial correlation function associated with the illuminating field. For coherent source, $h_i(r)$ is a constant, and the $\phi_i(r)$ and $\varphi(r)$ have the same profile. However, if the illumination is completely incoherent, $h_i(r)$ reduces to a delta function, and $\phi_i(r)$ becomes 0. Therefore, in principle, illumination can be set to approach a coherence area larger than the FOV to minimize the artifacts.
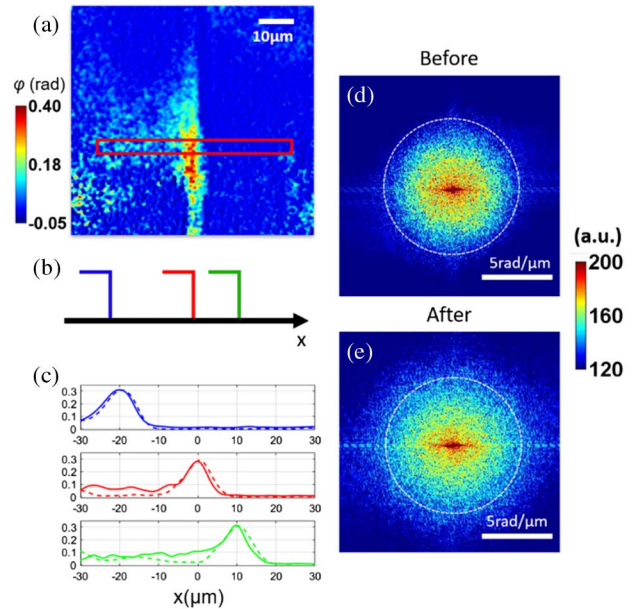

Fig. 3. System performance evaluation. The sample is a GaAs wafer with a rectangular pattern. (a) Typical step function response. (b) By moving the step along the x axis, one can obtain the response at every location. (c) Profiles of edge response at three positions before (dash lines) and after (solid lines) aberration correction. (d) Power spectrum of the phase image of an edge in (a) before aberration correction, and more high frequency appears after the correction (e).

Our measured edge responses at three different positions are shown in Fig. 3(c), which indicates that the eDPM system gives drastically different responses at different spatial locations, i.e., it is not a shift invariant system, and the resolution of the system cannot reach the "ideal" diffraction limit.

In order to diminish the effect of aberration, we adapted a computational adaptive optics (CAO) algorithm [35]. Introduced by Adie et al., this method is able to digitally correct aberrations in broadband interferometric imaging techniques using Zernike polynomials [36]. This approach is exploiting the complex field data, for which one can numerically access the (complex-valued) Fourier domain and, specifically, the spectral phase, which contains all information about geometric aberrations. To implement this algorithm, we first take the Fourier transform of the aberrated image, $\varphi(x, y)$, and obtain its frequency-domain representation, $\varphi(k_x, k_y)$. Here, we use the same symbol but different argument to distinguish the image and its Fourier transform. The corrected image, $\varphi_c(x, y)$, is obtained by using an optimal correction term in the spectral phase $h(k_x, k_y)$, which can be written as a linear combination of Zernike polynomials:

$$h(k_x, k_y) = \sum_n c_n \psi_n(k_x, k_y), \qquad (5)$$

where c_n the weighting factor, and ψ_n the nth Zernike mode. Thus, the measured phase image, φ, is modified to yield the corrected phase, φ_c, as

$$\varphi_c(x, y) = \mathfrak{F}^{-1}[\varphi(k_x, k_y) \exp(-ih(k_x, k_y))]. \qquad (6)$$

We implemented an iterative searching algorithm to automatically find the optimal value of c_n, as described in Ref. [37]. As shown in the solid lines in Fig. 3(c), the edge's response decays faster aberration corrections, and this improvement can also be observed from the frequency representation in the Fourier domain [Figs. 3(d) and 3(e)], where higher frequency components filled in the NA after correction.

To demonstrate the performance of this system, we started by measuring a purely reflective sample. We imaged a GaAs wafer with the UIUC letters etched on, the results of which are shown in Fig. 4. Compared to the raw phase map [Fig. 4(a)], the aberration-corrected image [Fig. 4(b)] has significantly lower noise in the background. We selected a
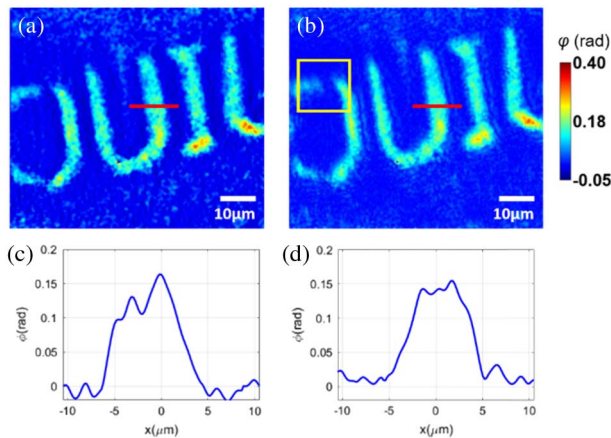
region on the sample indicated by the red line in both Figs. 4(a) and 4(b), and plotted the line profile of the corresponding region in Figs. 4(c)–4(d). As can be seen, the corrected phase image has a more uniform signal distribution and shaper edges, while the phase value is maintained. However, in regions away from the image center, the corrected result appears to be more blurred than the input [yellow box in Fig. 4(b)]. Because of the system spatially dependent response, it is impossible to use one set of weighting factors to fix aberrations across a large FOV. Our results show that the aberration correction tool works well in the central region (50 μm × 50 μm).

Next, to illustrate potential of eDPM for cellular imaging, we imaged white blood cells (WBCs) smeared on a glass slide. The sample preparation is described in Refs. [38,39]. Before the measurement, the cover slip of the blood smear was removed to avoid light reflection from the top glass surface. Figure 5(a) shows the reconstructed phase map and its power spectrum, respectively. Individual WBCs could be easily identified from the background, while the shapes of the cells appear distorted due to aberration. After applying the optimized phase filter [Fig. 5(c)], the cell shapes of these WBCs were restored [Fig. 5(d)]. The whole FOV is approximately 50 μm × 50 μm.

In summary, we developed a novel endoscopic QPI system. By attaching a DPM module to a GRIN-lens-based endoscope probe, our system enables single-shot, cell level resolution, endoscopic phase imaging. Using an objective lens to transfer the frequency content rather than the FOV provides higher resolution, at the expense of FOV. By appropriate spectral phase filtering, we numerically corrected the aberrations in the imaging system. Our measurements on a semiconductor and blood cells prove the capabilities of the proposed techniques. These preliminary results prove the capabilities of using QPI to map superficial biological structures in vivo. In order to prove the principle concept, this eDPM uses commercial elements. As a result, the accumulation of geometric aberration certainly affects the resolution, which is quantified in Fig. 3. Second, the endoscope system employs a halogen lamp as illumination. Though this broadband light source removes speckles in the phase image, a considerable level of chromatic aberration is introduced when light transmits through the GRIN lens.
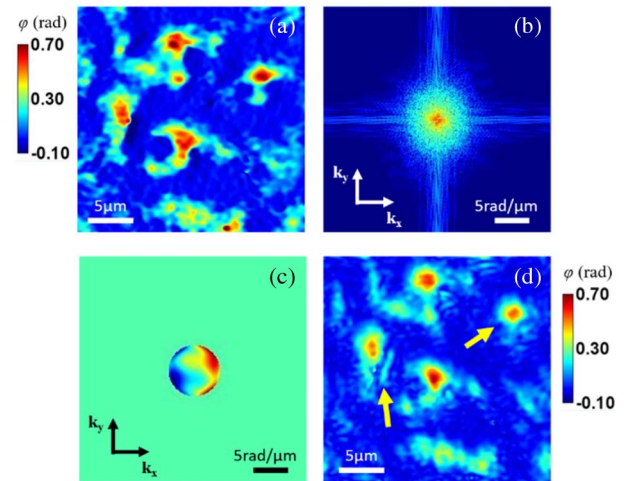
Fig. 4. eDPM image of GaAs wafer with UIUC letters. (a) Raw DPM phase map. (b) Aberration-corrected phase map. The respective line profiles are plotted in (c) and (d).

Fig. 5. Measurement of WBCs. (a) Aberrated image of WBCs. (b) Power spectrum of the image in (a). (c) Zernike polynomials with optimized weighting factors. (d) Aberration-corrected image.

Finally, the accuracy of the phase map in the DPM setup is strongly related to the spatial coherence of the source light. The illumination scheme in this setup causes a reduction of the measured value [34]. To improve the current drawbacks, replacing off-the-shelf elements with custom design is required, which is the goal for our future research. For *in vivo* studies, weak reflection from live tissue poses a potential challenge. We anticipate that one idea is to use an endoscope in "contact" with the tissue, so the spatial filtering will mostly provide that specular reflection. This way, the backscattering from tissue is amplified by the specular field that acts as a reference.

REFERENCES

1. R. Weissleder and V. Ntziachristos, Nat. Med. **9**, 123 (2003).
2. C. Balas, Meas. Sci. Technol. **20**, 104020 (2009).
3. H. S. Zeng, A. McWilliams, and S. Lam, Photodiagn. Photodyn. Ther. **1**, 111 (2004).
4. M. Filip, S. Iordache, A. Saftoiu, and T. Ciurea, World J. Gastroenterol. **17**, 9 (2011).
5. R. T. Kester, N. Bedard, L. Gao, and T. S. Tkaczyk, J. Biomed. Opt. **16**, 056005 (2011).
6. L. Fu and M. Gu, J. Microsc. **226**, 195 (2007).
7. M. T. Myaing, D. J. MacDonald, and X. Li, Opt. Lett. **31**, 1076 (2006).
8. D. R. Rivera, C. M. Brown, D. G. Ouzounov, I. Pavlova, D. Kobat, W. W. Webb, and C. Xu, Proc. Natl. Acad. Sci. USA **108**, 17598 (2011).
9. J. M. Yang, C. Favazza, R. M. Chen, J. J. Yao, X. Cai, K. Maslov, Q. F. Zhou, K. K. Shung, and L. H. V. Wang, Nat. Med. **18**, 1297 (2012).
10. M. C. Finlay, C. A. Mosse, R. J. Colchester, S. Noimark, E. Z. Zhang, S. Ourselin, P. C. Beard, R. J. Schilling, I. P. Parkin, I. Papakonstantinou, and A. E. Desjardins, Light Sci. Appl. **6**, e17103 (2017).
11. G. J. Tearney, M. E. Brezinski, B. E. Bouma, S. A. Boppart, C. Pitris, J. F. Southern, and J. G. Fujimoto, Science **276**, 2037 (1997).
12. K. Vishwanath and N. Ramanujam, *Encyclopedia of Analytical Chemistry* (Wiley, 2011).
13. J. A. Izatt, M. R. Hee, G. M. Owen, E. A. Swanson, and J. G. Fujimoto, Opt. Lett. **19**, 590 (1994).
14. B. E. Bouma and G. J. Tearney, *Handbook of Optical Coherence Tomography* (Marcel Dekker, 2002).
15. G. Popescu, *Quantitative Phase Imaging of Cells and Tissues* (McGraw-Hill Professional, 2011).
16. P. Marquet, B. Rappaz, P. J. Magistretti, E. Cuche, Y. Emery, T. Colomb, and C. Depeursinge, Opt. Lett. **30**, 468 (2005).
17. N. T. Shaked, L. L. Satterwhite, M. J. Telen, G. A. Truskey, and A. Wax, J. Biomed. Opt. **16**, 030506 (2011).
18. B. Kemper and G. von Bally, Appl. Opt. **47**, A52 (2008).
19. M. Shan, M. E. Kandel, and G. Popescu, Opt. Express **25**, 1573 (2017).
20. T. H. Nguyen, M. E. Kandel, M. Rubessa, M. B. Wheeler, and G. Popescu, Nat. Commun. **8**, 210 (2017).
21. F. Charriere, A. Marian, F. Montfort, J. Kuehn, T. Colomb, E. Cuche, P. Marquet, and C. Depeursinge, Opt. Lett. **31**, 178 (2006).
22. K. Kim, Z. Yaqoob, K. Lee, J. W. Kang, Y. Choi, P. Hosseini, P. T. C. So, and Y. Park, Opt. Lett. **39**, 6935 (2014).
23. Y. Park, M. Diez-Silva, G. Popescu, G. Lykotrafitis, W. Choi, M. S. Feld, and S. Suresh, Proc. Natl. Acad. Sci. USA **105**, 13730 (2008).
24. G. Popescu, Y. Park, N. Lue, C. Best-Popescu, L. Deflores, R. R. Dasari, M. S. Feld, and K. Badizadegan, Am. J. Physiol. **295**, C538 (2008).
25. W. J. Eldridge, Z. A. Steelman, B. Loomis, and A. Wax, Biophys. J. **112**, 692 (2017).
26. P. Girshovitz and N. T. Shaked, Biomed. Opt. Express **3**, 1757 (2012).
27. Y. Choi, C. Yoon, M. Kim, T. D. Yang, C. Fang-Yen, R. R. Dasari, K. J. Lee, and W. Choi, Phys. Rev. Lett. **109**, 203901 (2012).
28. K. Kim, K. Choe, I. Park, P. Kim, and Y. Park, Sci. Rep. **6**, 33084 (2016).
29. T. Cizmar and K. Dholakia, Nat. Commun. **3**, 1027 (2012).
30. B. Bhaduri, H. Pham, M. Mir, and G. Popescu, Opt. Lett. **37**, 1094 (2012).
31. S. Zhu, P. Jin, R. Liang, and L. Gao, Opt. Eng. **57**, 023110 (2018).
32. B. Bhaduri, C. Edwards, H. Pham, R. J. Zhou, T. H. Nguyen, L. L. Goddard, and G. Popescu, Adv. Opt. Photon. **6**, 57 (2014).
33. C. Edwards, B. Bhaduri, B. G. Griffin, L. L. Goddard, and G. Popescu, Opt. Lett. **39**, 6162 (2014).
34. T. H. Nguyen, C. Edwards, L. L. Goddard, and G. Popescu, Opt. Express **24**, 11683 (2016).
35. N. D. Shemonski, F. A. South, Y. Z. Liu, S. G. Adie, P. S. Carney, and S. A. Boppart, Nat. Photonics **9**, 440 (2015).
36. S. G. Adie, B. W. Graf, A. Ahmad, P. S. Carney, and S. A. Boppart, Proc. Natl. Acad. Sci. USA **109**, 7175 (2012).
37. P. Pande, Y. Z. Liu, F. A. South, and S. A. Boppart, Opt. Lett. **41**, 3324 (2016).
38. M. Mir, K. Tangella, and G. Popescu, Biomed. Opt. Express **2**, 3259 (2011).
39. M. Mir, H. F. Ding, Z. Wang, J. Reedy, K. Tangella, and G. Popescu, J. Biomed. Opt. **15**, 027016 (2010).